Quantification of coronary arterial stenoses in CTA using fuzzy distance transform

Yan Xu [a,b,c], Guoyuan Liang [a,b], Guangshu Hu [d], Yan Yang [e], Jinzhao Geng [f], Punam K. Saha [a,b,*]

[a] *Department of Electrical & Computer Engineering, University of Iowa, Iowa, IA 52240, United States*
[b] *Department of Radiology, University of Iowa, Iowa, IA 52240, United States*
[c] *School of Biological Science and Medical Engineering, Beihang University, Beijing, 100191, China*
[d] *Department of Biomedical Engineering, Tsinghua University, Beijing, 100084, China*
[e] *Department of Biomedical Engineering, Georgia Institute of Technology, Atlanta, GA 30332, United States*
[f] *The No. 1 Hospital, Tsinghua University, Beijing 100084, China*

ABSTRACT

Quantification of coronary arterial stenoses is useful for the diagnosis of several coronary heart diseases. Being noninvasive, economical and informative, computed tomographic angiography (CTA) has become a common modality for monitoring disease status and treatment effects. Here, we present a new method for detecting and quantifying coronary arterial stenosis in CTA using fuzzy distance transform (FDT) approach and a new coherence analysis of observed data for computing expected local diameter. FDT allows computing local depth at each image point in the presence of partial voluming and thus, eliminates the need for binarization, commonly, associated with inclusion of additional errors. In the current method, coronary arterial stenoses are detected and their severities are quantified by analyzing FDT values along the medial axis of an arterial tree obtained by its skeletonization. A new skeletal pruning algorithm has been developed toward improving the quality of medial axes and thereby, enhancing the accuracy of stenosis detection and quantification. Further, we have developed a new method to estimate "expected diameter" along a given arterial branch using a new coherence analysis of observed diameter values along the branch. The overall method is completed in the following steps – (1) fuzzy segmentation of coronary artery in CTA, (2) FDT computation of coronary arteries, (3) medial axis computation, (4) estimation of observed and expected diameters along arteries and (5) detection of stenoses and quantification of arterial blockage. The performance of this method has been quantitatively evaluated on a realistic coronary artery phantom dataset with randomly simulated stenoses and the results have been compared with a binary distance transform based and a conventional binary algorithm. The method has also been applied on a clinical CTA dataset from thirteen heart patients and the results have been compared with an expert's quantitative assessment of stenoses. Results of the phantom experiment indicate that the new method (error: 0.53%) is significantly more accurate as compared to both binary distance transform based (error 2.11%) and conventional binary (error 3.71%) methods. Also, the results of the clinical study indicate that the new FDT-based method (kappa coefficient = 87.9%) is highly in agreement with the expert's assessments and, in this respect, outperforms the other two methods (kappa coefficients = 75.2% and 69.5%).

© 2011 Elsevier Ltd. All rights reserved.

1. Introduction

Quantification of stenoses in coronary arteries is highly effective and often essential for the diagnosis of several coronary heart diseases [1–5]. Recent advancements of medical imaging techniques [6] have opened avenues for noninvasive imaging for diagnosis and treatment monitoring of several diseases. Computed tomo-graphic angiography (CTA) has become a commonly recommended imaging modality for clinical diagnostic purposes in different heart diseases, especially, for quantification of coronary arterial stenosis [2–5,7–11]. Research efforts have been devoted toward segment-ing coronary arterial trees [12–18] and quantification of stenoses [4,16,19–22] via CTA. Riedel et al. [12] developed a topology adap-tive active surface model for segmenting coronary arterial tree via CTA using a priori knowledge of vessel geometry and locally adaptive gray-scale statistics. Florin et al. [13] presented another coronary artery tree segmentation method via CTA using particle filtering and a Monte-Carlo sampling rule with parallel propaga-tion of multiple hypotheses dealing with bifurcations and multiple branches. Szymczak et al. [14] adopted a topological approach of

* Corresponding author at: Department of Electrical & Computer Engineering, University of Iowa, Iowa, IA 52240, United States. Tel.: +1 319 335 6420; fax: +1 319 335 6028.
E-mail address: pksaha@engineering.uiowa.edu (P.K. Saha).

extracting a connected forest of persistent maxima in a CTA image and the coronary artery trees were segmented from the forest using a geometric filtering. Yang et al. [15,17] developed a hybrid strategy for automatic segmentation of coronary arteries using multi-scale filtering and a Bayesian probabilistic approach within the level set segmentation model. Wang et al. [18] presented a vessel tree segmentation method by optimizing a "virtual contrast injection" algorithm using fuzzy connectivity [23–27]. Lesage et al. [28] presented a thorough review of state-of-the-art methods on vascular segmentation and analyzed different methods along three different axes, namely, models, features and extraction schemes. Also, they discussed the theoretical and practical properties of recent approaches and highlighted the most advanced and promising ones.

Current methods for the quantification of coronary arterial stenosis via CTA vary in their performance and the amount of user intervention required. Antiga et al. [19,20] used a 3D level set approach to segment arteries from CTA images and compute the maximal sphere inscribed inside a binary vascular region for stenosis quantification. Chen and Molloi [21] developed another algorithm for automatic quantification of coronary arterial stenosis using skeletonization and geometric analysis of branch length, diameter and bifurcation angles. Boskamp et al. [22] developed a research software tool for visualization and quantitative analysis of vessels and stenosis in CTA data sets using different morphological filtering, skeletonization and interactive masking. Yang et al. [16] developed a harmonic function to extract the centerline of tubular-tree structure and combined it with local cross-sectional area for detection and quantification of arterial stenosis. Blackmon et al. [10] presented an automated volumetric plaque analysis algorithm to measure non-calcified plaque burden in coronary CT angiography using centerline computation, thresholding and manual identification of lesions and adjustment of vessel diameters above and below the lesion. They have observed a high reproducibility of plaque measurements among experienced and inexperienced observers. Cordeiro et al. [7] proposed a modified automatic 3D approach using manual vessel isolation and different window or level settings and semi-automatic centerline detection to evaluate ≥50% stenoses. They have observed that the modified automatic 3D method is equivalent to and significantly less time consuming than traditional manual 2D methods. Recently, a thorough survey of coronary CTA based stenosis detection and quantification methods including automated measures has been reported in [11]. Manual plaque labeling using multi-planar formatting [8,9] is popularly used in clinical studies to detect and quantify coronary stenoses.

Despite radical advancements in CTA technology, limited signal-to-noise ratio (SNR) and resolution, currently achievable in clinical scans, leads to significant partial voluming effect, especially, for small-scale structures like an arterial tree. Therefore, "hard decision" such as binarization should preferably be avoided or delayed to the very end of a coronary stenoses detection and quantification processing chain. Here, we introduce a method that obviates binary segmentation and effectively handles partial voluming effects in images at currently achievable resolution regime.

The method of detecting and quantifying coronary arterial stenosis in CTA utilizes fuzzy distance transform (FDT) approach and a new coherence analysis of observed data for computing expected local diameter. Specifically, FDT [29] used to achieve sub-voxel accuracy which is instrumental in early detection of diseases. Ordinary distance transform (DT) [30–35] requires a binary segmentation of an object in an image and is based on finding a shortest distance measure from the background. DT has been popularly adopted in many digital geometric applications [36] of binary objects. Borgefors [33–35] extensively studied DTs for binary 3D objects and presented the integer-valued approximation of the

optimal local step lengths that are widely used by others. Local step optimization and accuracy of DT has further been studied by other research groups [37–39]. Recently, Saha et al. [29] have introduced a generalized fuzzy distance transform and established its metric property. Applications of FDT have been investigated by different research groups [40–44]. Effectiveness of FDT in measuring trabecular bone thickness at limited in vivo resolution regime has been shown [40,45–47]. Here, we adopt a similar approach for measuring local diameters along a coronary artery centerline and use these values for detecting and quantifying stenoses. Although, it is desirable to compute arterial centerline from its fuzzy representation, such developments demand significant new theoretical research related to topology and shape preservation in fuzzy objects. In the current work, binary representation of coronary artery is used for skeletonization. A comprehensive framework for evaluating centerline detection algorithms for coronary vasculature has been presented by Rotterdam coronary axis tracking evaluation group [48]. Another major challenge in automatic quantification of stenoses is how to determine expected diameters at different locations in an arterial tree. We have developed a new method to estimate "expected diameter" along a given arterial branch using a new coherence analysis of observed diameter values along the branch. This paper is organized as follows. In Section 2, we describe the theory and algorithms of individual steps involved in detection and quantification of coronary arterial stenoses. Section 3 presents our experimental setup and methods evaluating the new stenosis detection and quantification algorithm. Finally, experimental results and discussion are presented in Section 4.

2. Theory and algorithms

In this section, we describe the theory and algorithms for detection and quantification of coronary arterial stenoses. The method is completed in the following steps – (1) fuzzy segmentation of coronary artery in CTA, (2) FDT computation of coronary arteries, (3) medial axis computation, (4) estimation of expected and observed diameters along arteries and (5) detection of stenoses and quantification of arterial blockage. The first step is accomplished using a previously published method by Yang et al. [15,17] (see Section 3.2 for a short description). In the following, we describe the theory and algorithms of other steps involved in the current method.

2.1. Fuzzy distance transform [29]

A fuzzy subset S of any set S is a set of ordered pairs $S = \{(x, \mu_s(x))|x \in S\}$ whose first element is a member of the underlying regular set S and the second element $\mu_s: S \to [0,1]$, often, referred to as the membership function, yields the membership value of x in S. Throughout this paper, we will use script letters to denote fuzzy subsets and "μ" subscripted by the fuzzy subset to denote its membership function. A digital space [49] D is often represented as an ordered pair $D = (\mathbb{Z}^3, \alpha)$, where $\mathbb{Z}$ denotes the set of integers and $\mathbb{Z}^3$ represents the underlying "3-D cubic grid" (in short, "cubic grid"); also, α is a binary relation on $\mathbb{Z}^3$ indicating the adjacency between every two elements in $\mathbb{Z}^3$. An element of the cubic grid is referred to as a voxel and is represented by a triple of integer coordinates. In this paper, standard 26-adjacency [50] is adopted for α, i.e., two voxels (x_1, x_2, x_3) and (y_1, y_2, y_3) in $\mathbb{Z}^3$ are adjacent if and only if, $\max_{1 \leq i \leq 3} |x_i - y_i| \leq 1$, where $|\cdot|$ gives the absolute value. A 26-adjacent voxel of a voxel p is also referred to as a 26-neighbor of p; the set of all 26-neighbors of p excluding itself is denoted as $N_{26}(p)$. In the rest of this paper, by "adjacency" we will understand "26-adjacency" unless stated otherwise. A digital object O is a fuzzy subset $\{(p, \mu_O(p))|p \in \mathbb{Z}^3\}$ of

$\mathbb{Z}^3$. As pointed out earlier, the current application aims to compute both observed and expected diameters at each location along a coronary artery tree via CTA. Following our target application, a digital object O represents a fuzzily segmented coronary artery tree and at any voxel p, the membership value $\mu_O(p)$ represents the partial content of arterial lumen at p. The support $\Theta(O)$ of a digital object O is the set of all voxels with nonzero membership, i.e., $\Theta(O) = \{p | p \in \mathbb{Z}^3 \text{ and } \mu_O(p) \neq 0\}$.

A path π in a set S of voxels from $p \in S$ to $q \in S$ is a sequence $\langle p = p_0, p_1, \ldots, p_{n-1} = q \rangle$ of voxels in S such that every two successive voxels are adjacent. For the purpose of defining the length of a path, we use the notion of a "link" and its length. A link is simply a path $\langle p, q \rangle$ consisting of exactly two adjacent voxels $p, q \in \mathbb{Z}^3$. The length of a link $\langle p, q \rangle$ in a digital object O is calculated as $(1/2)(\mu_O(p) + \mu_O(q))\|p - q\|$, where $\|\cdot\|$ denotes any Euclidean L2 norm. The length of a path $\pi = \langle p_0, p_1, \ldots, p_{n-1} \rangle$ in a digital object O, denoted by $II_O(\pi)$, is defined as the sum of lengths of all links along the path, i.e.,

$$II_O(\pi) = \sum_{i=0}^{n-2} \frac{1}{2}(\mu_O(p_i) + \mu_O(p_{i+1}))\|p_i - p_{i+1}\|.$$

Between any two voxels $p, q \in \mathbb{Z}^3$, there exist infinitely many paths; let $P(p, q)$ denote the set of all paths from p to q. A path $\pi_{p,q} \in P(p, q)$ is one of the shortest paths from p to q in O, if and only if, for all $\pi \in P(p, q)$. The fuzzy distance between two voxels $p, q \in \mathbb{Z}^3$ (which are not necessarily distinct), denoted by $\omega_O(p,q)$ or $\omega_O(q,p)$, is the length of one of the shortest paths from p to q, i.e.,

$$\omega_O(p, q) = \omega_O(q, p) = \min_{\pi \in P(p,q)} II_O(\pi).$$

Theorem 1. *For any digital space $D = (\mathbb{Z}^3, \alpha)$, for any digital object O on D, the fuzzy distance ω_O is a metric over the support $\Theta(O)$ of O.*

The above theorem states the metric property of fuzzy distance; a proof of this theorem is available in [29]. The fuzzy distance transform or FDT of a digital object O is represented as an image $\{(p, \Omega_O(p)) | p \in \mathbb{Z}^3\}$, where $\Omega_O(p)$ denotes the FDT value at p which is the fuzzy distance between p and the nearest voxel in $\overline{\Theta}(O) = \mathbb{Z}^3 - \Theta(O)$. In other words,

$$\Omega_O(p) = \min_{q \in \overline{\Theta}(O)} \omega_O(p, q).$$

Finally, it may be noted that the FDT value at any voxel $p \in \overline{\Theta}(O)$ is always "0". In the following, we present an algorithm for computing FDT of a digital object.

begin compute_fuzzy_distance_transform

input: a digital object $\mathcal{O} = \{(p, \mu_O(p)) | p \in \mathbb{Z}^3\}$

output: the FDT image $\{(p, \Omega_O(p)) | p \in \mathbb{Z}^3\}$

auxiliary data structure: a sequential queue Q

Step1 **for** each voxel $p \in \Theta(\mathcal{O})$

          assign $\Omega_O(p) = max\_FDT\_value$

Step2 **for** each voxel $p \in \overline{\theta}(\mathcal{O})$

          assign $\Omega_O(p) = 0$

          if $N_{26}(p) \cap \Theta(\mathcal{O})$ is non-empty

                push p in Q

Step 3 **while** Q is not empty

          pop a voxel p from Q

          for each voxel $q \in N_{26}(p)$

                define $link(p,q) = \frac{1}{2}(\mu_O(p_i) + \mu_O(p_{i+1}))\|p - q\|$

                if $\Omega_O(q) > \Omega_O(p) + link(p,q)$

                      assign $\Omega_O(q) = \Omega_O(p) + link(p,q)$

                      push q in Q

end compute_fuzzy_distance_transform

The above algorithm computes FDT value at every voxel q using a wave propagation approach through a dynamic programming algorithm. The wave propagation process is initiated by setting a large value (i.e., the FDT value is currently unknown) inside the object region (Step 1) and by initiating waves at the background adjacent to the object region (Step 2); note that the queue Q keeps track of all active waves. In Step 3, these waves are taken out of Q one by one and propagated inside the object region through a dynamic programming approach and whenever the current FDT value at a voxel q is changed, a new wave is created and pushed into Q. Finally, the algorithm terminates when Q is exhausted.

2.2. Skeletonization

Here, we adopt a previously reported skeletonization algorithm [51]. It is clearly desirable to utilize the skeleton of an object directly computed from its fuzzy representation by taking into account the fuzzy membership value at each voxel. However, such an approach demands significant additional research developments, which are beyond the scope of the current paper. We therefore applied the binary skeletonization to the support $\Theta(O)$ of an object O to obtain its medial axis representation by selecting the method reported by Saha et al. [51] which is further improved here by incorporating a new noise-pruning algorithm described hereafter. It may be noted that no explicit threshold is required to define the support $\Theta(O)$ and therefore, the resulting skeleton is not threshold sensitive.

The method by Saha et al. [51] completes the skeletonization process in two steps, namely, surface skeletonization and curve skeletonization. Again, each of the surface and curve skeletonizations is accomplished in two steps – primary skeletonization and secondary skeletonization. Primary surface skeletonization iteratively erodes object voxels from the current outer layer while preserving the topology and so-called "shape" of an object. The authors introduced the notions of s-, e-, and v-open voxels and processed those voxels separately to better preserve the geometry of different types of corners in an object [51]. In order to preserve object topology, only simple voxels [52] are considered for erosion. A voxel p is a simple voxel if its deletion preserves the topology of the object and it has been shown that a voxel is a simple voxel [52,53] if and only if the number of objects $\xi(p)$ in $N_{26}(p)$ is '1' and the number of tunnels $\eta(p)$ and that of cavities $\delta(p)$ in $N_{26}(p)$ are both zero (see Saha and Rosenfeld [49] for definitions of tunnels and cavities). Both surface- and arc-like shape voxels [51] are preserved during the erosion process. The output of primary surface skeletonization, as described in [51], may include two-voxel thick surfaces and curves. These extra thick voxels are subsequently eliminated using an extra iteration which is referred to as secondary surface skeletonization. Primary curve skeletoniza-
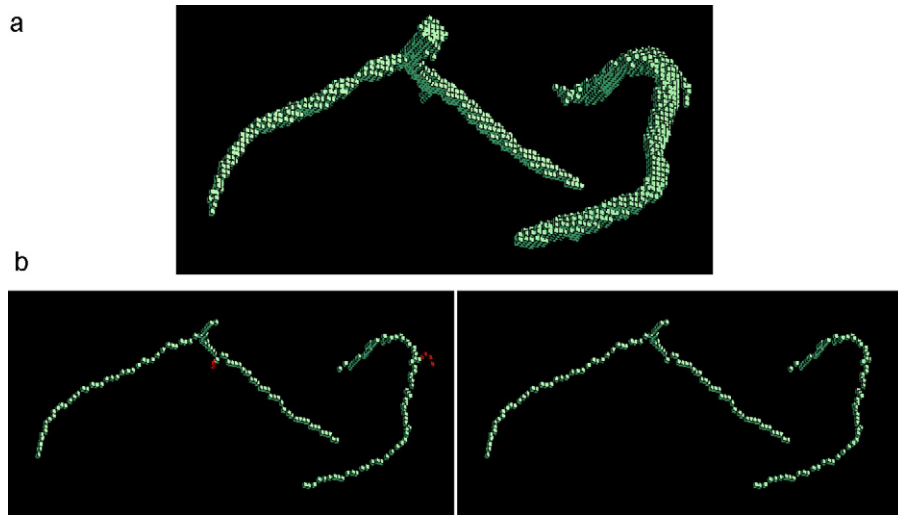
Fig. 1. Results of curve skeletonization and noise pruning. (a) A region from a binarized coronary artery tree. (b) Curve skeleton of (a) without noise pruning; voxels identified as noise using the proposed post-skeletonization noise pruning algorithm are colored in red. (c) The result after noise pruning.

tion is a process similar to primary surface skeletonization where surface skeletal voxels are iteratively eroded along surface edges while preserving the topology and shape of the surface. Unlike surface skeletonization, here only arc-like shape voxels are preserved; finally, two-voxel thick curve voxels [51] are removed during the secondary curve skeletonization. It may be noted that, surface skeleton produced a digital structure consisting of both arcs and surfaces. These arcs need no further thinning while the surfaces are converted into arcs during arc-skeletonization (see Fig. 10 in [51]).

The output of curve skeletonization is presented in Fig. 1(b); although, the method attempts to reduce the effects of noise in the skeleton, it does so using only the local context of object geometry and therefore, is bound to fail in a larger context. Here, we present a new post-skeletonization algorithm to identify and eliminate noisy branches in a skeleton. Unlike, the noise removal approaches, commonly adopted in a skeletonization algorithm, the current method defines noise in a global context of skeletal geometry. Let S denote the set of all voxels in a surface/curve skeleton. Although, the method is applied here on curve skeletons of arterial trees, it is equally applicable to a surface skeleton. The basic idea here is to distinguish skeletal branches contributed by true geometric features in the original object from those originated by noisy bumps or dents common in digital images. However, a small branch originating from a one- or two-voxel protrusion may grow iteratively due to the topology preservation constraint and eventually leading to a long branch in the final skeleton (see Fig. 2). Frequently, such branches appear to be an important feature in a skeleton and may not be recognized as a noisy branch without additional information. To overcome this problem, in a skeletal branch, we distinguish voxels needed to maintain object shape features from those survived merely for topology preservation. Fortunately, the skeletonization method adopted here keeps record of the voxels surviving for shape preservation during skeletonization; we will refer to those voxels as shape voxels in a skeleton and will use S_S to denote the set of all shape voxels in the skeleton S. In order to determine the importance of a branch in a skeleton, we only consider shape voxels in length computation and ignore voxels survived merely for topology preservation. The idea of shape distance transform (STD) may be better understood using an example as illustrated in Fig. 2. Let us consider a linear digital shape as shown in the figure that contains a noisy pixel. Following that shape pixels/voxels are always defined locally, a noisy pixel/voxel may slip through the constraint of a shape pixel/voxel. Depending upon the constraints for a shape
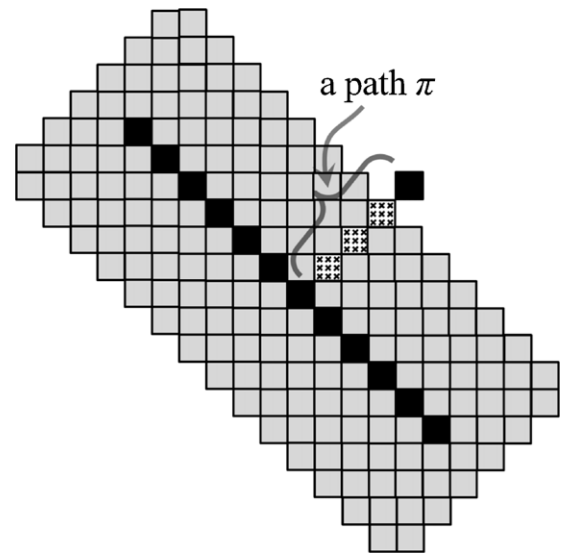

Fig. 2. An illustration of shape distance transform. Both black and textured pixels indicate skeletal pixels in the given shape. Black pixels survive in the skeletonization process as shape pixels, i.e., saved to preserve local shape of the structure. On the other hand textured pixels are preserved to maintain the topology. Shape distance only counts shape voxels on a path. For example, only one shape voxel contributes to the shape length of the path π.

point, it is always possible to create an example of a noisy protrusion that is wrongly chosen as a shape pixel/voxel. Here, we have used a simple example as our main intention is to illustrate the idea of *SDT*. Although, only one pixel in a noisy protrusion is selected as a shape pixel, it leads to a long branch in the final skeleton caused by topology preservation. Therefore, just by looking at the skeleton, it is often difficult to decide whether a branch is caused by noisy protrusion or it carries meaningful information of the original shape. We formulate *SDT* such that only shape pixels/voxels contribute to the "shape length" of a path (or a branch) and the pixels/voxels survived merely because of topology preservation are ignored. Thus only one pixel will contribute to shape length of the path π that later makes it easy to decide the path as a noisy branch. Shape length is formulated using a new membership function μ_{S_S} which takes '1' value when a voxel is a shape voxel and '0', otherwise.

Using the digital topological classification method [50], we can identify junction, interior and edge voxels in a skeleton. Let S_E

denote the set of all edge voxels and let S_J denote the set of all junction voxels in the skeleton S. A 26-path $\pi = \langle p = p_0, p_1, \ldots, p_{n-1} = q \rangle$ between two voxels $p, q \in S$ is called a 26-valid path in S if $\nexists r \in S_j$ and $0 \leq i < n$ such that $\|p_i - p_{i+1}\| > \max(\|p_i - r\|, \|r - p_{i+1}\|)$. A violation of the validity condition of a path is considered as a "crossing" with a junction, because, the path $\ldots, p_i, r, p_{i+1}, \ldots$ is more natural than the path $\ldots, p_i, p_{i+1}, \ldots$ in the sense that the former path requires shorter steps to move from p_i to p_{i+1}. Shape length of any 26-valid path $\pi = \langle p_0, p_1, \ldots, p_{n-1} \rangle$ on a skeleton S, denoted by $II_{S_S}(\pi)$ is defined as follows

$$II_{S_S}(\pi) = \sum_{i=o}^{n-2} \frac{1}{2}(\mu_{S_S}(p_i) + \mu_{S_S}(p_{i+1}))\|p_i - p_{i+1}\|,$$

where

$$\mu_{S_S}(p) = \begin{cases} 1, & \text{if } p \in S_S, \\ 0, & \text{otherwise.} \end{cases}$$

Shape distance transform or *SDT* of a voxel $p \in S$, denoted by $SDT(p)$ is the shape length of one of the shortest (w.r.t. shape length) 26-valid paths from p to any voxel $q \in S_E$; if there is no 26-valid path from p to a voxel $q \in S_E$, the *SDT* value $SDT(p)$ is set to $+\infty$ or equivalently, a very large number. The algorithm for computing shape distance transform is presented in the following.

begin compute_shape_distance_transform

input: (1) a skeleton S

　　　　　　(2) a set of junction voxels $S_J \subset S$

　　　　　　(3) a set of edge voxels $S_E \subset S$

　　　　　　(4) a set of shape voxels $S_S \subset S$

　　　　　　(5) a fuzzy distance transform image $\{(p, \Omega_O(p)) | p \in \mathbb{Z}^3\}$

output:　　　shape distance transform map $SDT: S \rightarrow \Re$

auxiliary data structure: a sequential queue Q

Step 1 for each voxel $p \in S$

　　　　　　assign $SDT(p) = max\_SDT\_value$

Step 2 for each voxel p in S_E

　　　　　　assign $SDT(p) = \Omega_O(p)$

　　　　　　push p in Q

Step 3 while Q is not empty

　　　　　　pop a voxel p from Q

　　　　　　for each voxel $q \in N_{26}(p) \cap S$

　　　　　　　　　define $link(p,q) = \frac{1}{2}\left(\mu_{S_S}(p_i) + \mu_{S_S}(p_{i+1})\right)\|p - q\|$

Step 3a　　　　　**if** $q \in S_J$ AND $SDT(q) > SDT(p) + link(p,q)$

　　　　　　　　　assign $SDT(q) = SDT(p) + link(p,q)$

Step 3b　　　　　**else if** $SDT(q) > SDT(p) + link(p,q)$

　　　　　　　　　AND $\nexists r \in S_J$ such that $\|p - q\| > \max(\|p - r\|, \|q - r\|)$

　　　　　　　　　assign $SDT(q) = SDT(p) + link(p,q)$

　　　　　　　　　push q in Q

end compute_shape_distance_transform

The above algorithm for computing shape distance transform works similar as the FDT computation algorithm except that initial waves are placed only at edge voxels of a skeleton (Step 2). Also, in the wave propagation process (Step 3), only shape voxels contribute in shape distance as discussed earlier. The conditions in Steps 3a and b are used to check validity of paths to avoid undesired crossing with junctions.

The noise pruning is accomplished using the following algorithm where noisy branches are unglued at junctions by removing all voxels around junctions with SDT value less than a threshold. Step 2 defines seed voxels with STD value above the threshold and Step 3 allows it to grow the skeleton over the region with noise branches unglued at Step 1.

begin compute_noise_pruning

input: (1) a skeleton S

(2) a set of junction voxels $S_J \subset S$

(3) shape distance transform map $SDT : S \rightarrow \Re$, and

(4) a predefined threshold thr

output: noise pruned skeleton S'

assign a temporary skeleton $tS = S$

Step 1 **for** each voxel $p \in S_J$

    for each voxel $q \in N_{26}(p) \cap S - S_J$

        if $SDT(q) < thr$

            assign $tS = tS - \{q\}$

Step 2 assign a set of seed voxels S_d as follows

$$S_d = \{p | p \in tS \text{ and } SDT(p) \geq thr\}$$

Step 3 assign the noise pruned skeleton S' as follows

$$S' = \{p | p \in tS \text{ and } p \text{ is 26-connected to } S_d \text{ in } tS\}$$

end compute_noise_pruning

The result of noise pruning is illustrated in Fig. 1(c); all voxels identified as noisy voxels are colored in red in the original curve skeleton in Fig. 1(b). Here, we have used $thr = 3$ voxel units. Performance of our arc skeletonization algorithm has been evaluated using the eight training datasets from the Rotterdam coronary axis tracking evaluation framework [48] available online (http://coronary.bigr.nl/) and the results are presented in Table 1. The performance of the skeletonization algorithm is satisfactory.

2.3. Computation of expected and observed arterial diameters

As mentioned earlier, our stenosis detection/quantification algorithm is essentially based on comparing between expected and observed diameters of arterial lumen along the arterial tree. In this paper, we use "arterial diameter", "lumen diameter", and "arterial lumen diameter" synonymously and "arterial blockage" to indicate

Table 1
Average values and scores for overlap (OA), overlap until first error (OF), overlap with clinically relevant part of the vessel (OT) and average inside (AI) computed from eight training datasets following the Rotterdam coronary axis tracking evaluation framework.

Measure	Average	Score
OV (%)	90.1	72.7
OF (%)	71.2	61.5
OT (%)	89.3	68.6
AI (mm)	0.32	38.5

the inverse of "arterial diameter". FDT provides the depth mapping at each voxel within the support of a coronary arterial tree and the principle of FDT-based thickness computation is to sample depth values along the medial axis of coronary artery, thus, providing the regional thickness distribution along the artery. Here, this approach is adopted to compute "observed diameter" at each axial location along an arterial tree. Skeletonization is a widely used technique to generate a medial axis representation of an object. Therefore, the distribution of regional thickness is computed by sampling the FDT values along the curve skeleton of an artery.

Computation of "expected diameter" is more challenging as observed diameter is the only available information in CTA-based stenosis detection/quantification and it fails to provide a reliable measure of expected diameter around a diseased region which, in contrast, is the primary region of interest. Therefore, an algorithmic scheme for computing expected diameter needs to account for abnormalities in observed diameters. One possible solution [54] is to use the observed diameter at two end points of an arterial branch and determine the expected diameter elsewhere inside the branch using linear interpolation. However, a major disadvantage of this method is that, often, stenoses appear near bifurcations of arterial branches leading to a significant source of inaccuracies in measurement of expected diameter at branch endpoints. Here, we present a new method of computing expected diameters along an arterial branch using its observed data. Let $\langle p_0, p_1, \ldots, p_{n-1} \rangle$ denote the sequence of skeletal voxels along an arterial branch with p_0 and p_{n-1} being the two end points of the branch; let x_i denote the arc-length from p_0 to p_i along the skeletal branch. Let $D_{observed}(p)$ denote the observed arterial diameter at any skeletal voxel p. Fig. 3(a) illustrates a partial coronary arterial tree with no visible stenosis on the test branch. A plot of observed arterial diameter as a function of skeletal arc-length from p_0 is presented in Fig. 3(b) for the test branch. Fig. 3(c) and (d) illustrate the same as Fig. 3(a) and (b), respectively, but for an arterial branch with a visible stenosis. A preferred method of computing expected arterial diameter should be able to exclude the diameter values around a stenosis while capturing the statistical trend of diameter readings over healthy regions on the branch. Our method is based on coherence analysis of observed data along an arterial branch. Specifically, we find a set of a predefined number of mutually coherent observed diameters along an arterial branch and is accomplished by iteratively dropping a data-point most non-coherent with the current data-trend as presented in the following algorithm.
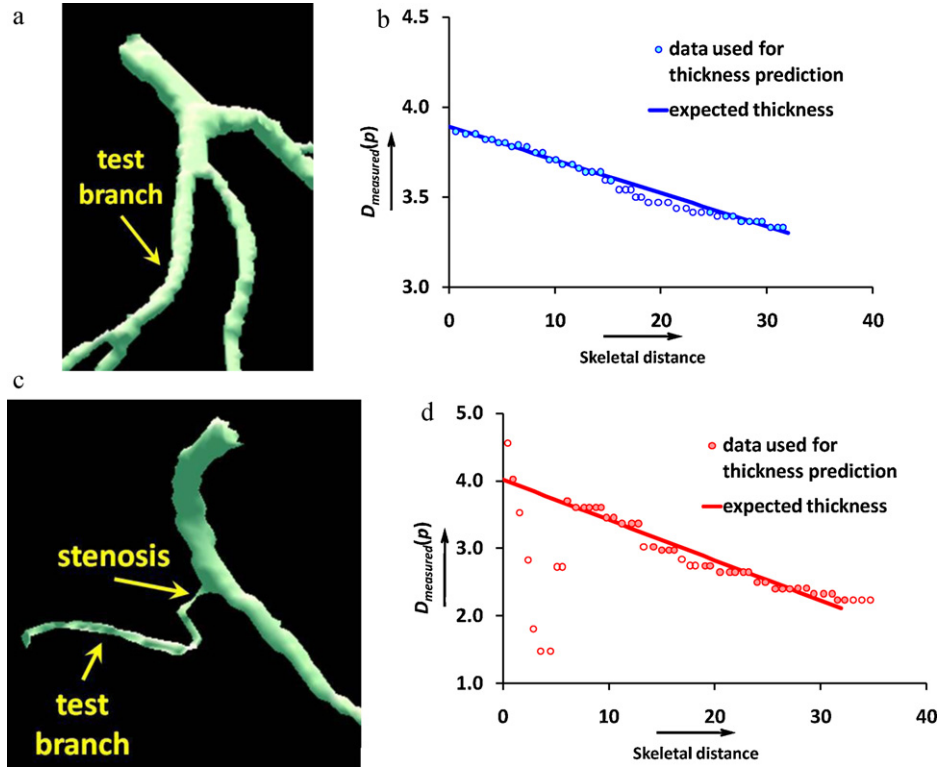
Fig. 3. (a and b) Results of expected arterial diameter computation on a healthy arterial branch. The straight line shown in (b) predicts the expected diameter at any location along the arterial branch. (c and d) Same as (a) and (b) but for a branch with a visible stenosis. It is notable in (d) that the method successfully eliminates the artifacts in observed diameters around the stenosis.

begin compute_expected_diameter

input: (1) a sequence $\langle p_0, p_1, \cdots, p_{n-1} \rangle$ of voxels along an arterial skeletal branch A

(2) skeletal arc-length x_i at each voxel p_i from the starting voxel p_0 along A

(3) observed arterial diameters $D_{\text{observed}}(p_i) | i = 0, 1, \cdots, n - 1$

(4) X: percentage of data-points to be excluded from final analysis

output: equation of a straight line $y = mx + c$ predicting expected arterial diameter along A where $y_i = mx_i + c$ yields the expected diameter at p_i

assign $P = \{p_0, p_1, \cdots, p_{n-1}\}$

assign $l = \lfloor nX/100 \rfloor$

compute the best-fit straight line $y = m_0 x + c_0$ from the set of points $\left\{ (x_i, D_{\text{observed}}(p_i)) | i = 0, 1, \cdots, n - 1 \right\}$

for $j = 1, 2, \cdots, l$

find the point p_k in P that is farthest to the straight line $y = m_{j-1} x + c_{j-1}$

assign $P = P - \{p_k\}$

compute the best-fit straight line $y = m_j x + c_j$ from the set of points $\left\{ (x, D_{\text{observed}}(p)) | p \in P \right\}$

output the straight line $y = m_l x + c_l$

end compute_expected_diameter

Although, the above method uses a linear model for diameter evaluation, a nonlinear model, e.g., an exponential model may be used within the same framework. Here, we have adopted a linear diameter evaluation, because of the computational simplicity. Results of application of the algorithm for computing expected diameter along the test branches indicated in Fig. 3(a) and (c) are presented in Fig. 3(b) and (d). It is notable in Fig. 3(d) that the algorithm has successfully dropped the points around the stenosis and thus eliminates effects of the depression in observed diameters caused by the stenosis. It ensures that the expected diameters are computed from observed diameters over healthy regions only.

Here we have used $X = 30$, i.e., the method uses the most coherent 70% of observed diameters along an arterial branch to compute its expected diameters. Our algorithm of computing expected arterial diameter has been found to be quite robust with the choice of X. The same algorithm was run with three different values of X and the equation of the final straight line predicting arterial diameters varied only minimally as follows:

Test branch of Fig. 3(a):

(a) $y = -0.0184x + 3.8895|_{x=30\%}$
(b) $y = -0.0181x + 3.8854|_{x=40\%}$
(c) $y = -0.0181x + 3.8856|_{x=50\%}$

Test branch of Fig. 3(b):

(a) $y = -0.0595x + 4.0202|_{x=30\%}$
(b) $y = -0.0606x + 4.0562|_{x=40\%}$
(c) $y = -0.0614x + 4.0846|_{x=50\%}$

Further, the method is presumed to be less sensitive to sudden changes in arterial diameter after bifurcation and the expected diameters along an arterial branch is computed from the measured diameters on the entire branch and not just at two ends.

2.4. Stenosis detection and quantification of arterial blockage

In coronary angiograms, "percent stenosis" is a widely used measure for lesions for assessing severity of arterial diseases. Percent stenosis is calculated by dividing the minimum lumen diameter (MLD) by a nearby "normal" or "reference" diameter. However, location of nearby "normal" lumen and computation of "reference" diameter are largely empirical and to some extent inaccurate, especially, in the presence of lesions. As a result, computed percent stenosis frequently underestimates the pathologically authentic stenosis. It has been reported [55] that the differences between computed percent stenosis and the authentic stenosis observed by pathologic tests may vary from 20% to 60%. To solve this problem, we have developed a new method, presented in Section 2.3, for computing expected diameter along an arterial branch that successfully drops the non-coherent diameter values around stenoses ensuring that expected diameters are determined from observed diameters over healthy regions only. Fractional occupancy of lumen at any voxel p on the curve skeleton or medial axis of an artery is defined as the ratio of its observed diameter $D_{observed}(p)$ and expected diameter $D_{expected}(p)$. The percentage of stenosis at p is computed using the following equation

$$stenosis(p) = \begin{cases} 0, & \text{if } D_{observed}(p) \geq D_{expected}(p), \\ 1 - \dfrac{D_{observed}(p)}{D_{expected}(p)}, & \text{otherwise.} \end{cases} \quad (1)$$

Effects of random errors in stenosis computation are reduced by applying a smoothing operation on the observed stenosis values along the arterial skeletal tree with a Gaussian kernel of $\sigma = 1.5$ voxel unit; in the rest of this paper, by "observed stenosis" we will refer to the value after the smoothing operation. A stenosis γ is defined as a set of 26-connected voxels p on the arterial curve skeleton with observed stenosis $(p) \geq 12.5\%$. Finally, the grade of a stenosis γ, denoted by $S(\gamma)$, is defined as the maximum observed stenosis among all voxels $p \in \gamma$, i.e., $S(\gamma) = \max_{p \in \gamma} stenosis(p)$. In this paper, we quantify severity of a stenosis into five different categories as follows:

0% stenosis: grade of the stenosis is less than 12.5%;
25% stenosis: grade of the stenosis is greater than equal to 12.5% but less than 37.5%;

50% stenosis: grade of the stenosis is greater than equal to 37.5% but less than 62.5%;
75% stenosis: grade of the stenosis is greater than equal to 62.5% but less than 87.5%;
100% stenosis: grade of the stenosis is greater than equal to 87.5%.

Although several separate narrowings may be present on the same arterial branch, only the most severe one is detected and others are ignored. An expected stenosis, known from the ground truth, and an observed stenosis are considered matching if they lie on the same arterial tree branch. Although the proposed definition of matching stenoses is a little generous, it simplifies the comparative evaluation between clinical experts and computerized algorithms as experts denote a stenosis address using branch name.

3. Methods and experimental setup

Two experiments have been conducted to examine the effectiveness of the proposed FDT-based stenosis quantification method. The first experiment is designed to evaluate the accuracy of the method based on realistic coronary artery phantom data with randomly simulated stenoses while the second one is aimed to assess the performance of the method on clinical setup. The performance of the new method was compared with two other methods:

(1) A classical binary algorithm [56] was implemented based on analyzing local cross-sectional area of the binarized artery-tree on a plane perpendicular to the centerline at that location; we will refer to it as a "conventional" method.
(2) A non-FDT version of the current new method was implemented with a standard binary distance transform (BDT) [30–35] and a standard skeletonization algorithm [51] followed by the same steps as in the current method; we will refer to it as the BDT-based method.

Both conventional and BDT-based methods were applied to the same dataset for detecting stenoses and grading them using the same protocol described in Section 2.4. In the following, we present data description, methods and the setup for each of the two experiments.

3.1. Simulated phantom experiment

Five healthy coronary artery tree phantoms were simulated following the method described by Leung et al. [57] to examine the accuracy of the proposed FDT-based stenosis detection and quantification method. Each simulated coronary arterial tree includes right coronary artery (RCA) and acute marginal (AM) in the right coronary tree and left main coronary artery (LM), proximal left anterior descending artery (LAD), first diagonal (FD), second diagonal (SD) and proximal left circumflex artery (LC) in the left coronary tree; an example of a healthy phantom is presented in Fig. 4(a). Normal diameter of each branch in the right and left coronary tree was assigned according to the average diameter values recommended by Chalopin et al. [58]. On a given healthy phantom, a stenosis was simulated using a sinusoidal depression model [59] in arterial diameters along the skeletal line of an arterial branch. The width of a stenosis was randomly selected over 10–25% of corresponding branch length. In order to generate the effects of blurring, each original image was generated at high resolution of $0.143 \times 0.143 \times 0.417 \, mm^3$ which was down sampled at $0.43 \times 0.43 \times 1.25 \, mm^3$ yielding a fuzzy representation. Further, an additive Gaussian random noise of SNR 10 was subjected to each down sampled image to obtain a final simulated data for test. An example of a test phantom with simulated stenoses of varying
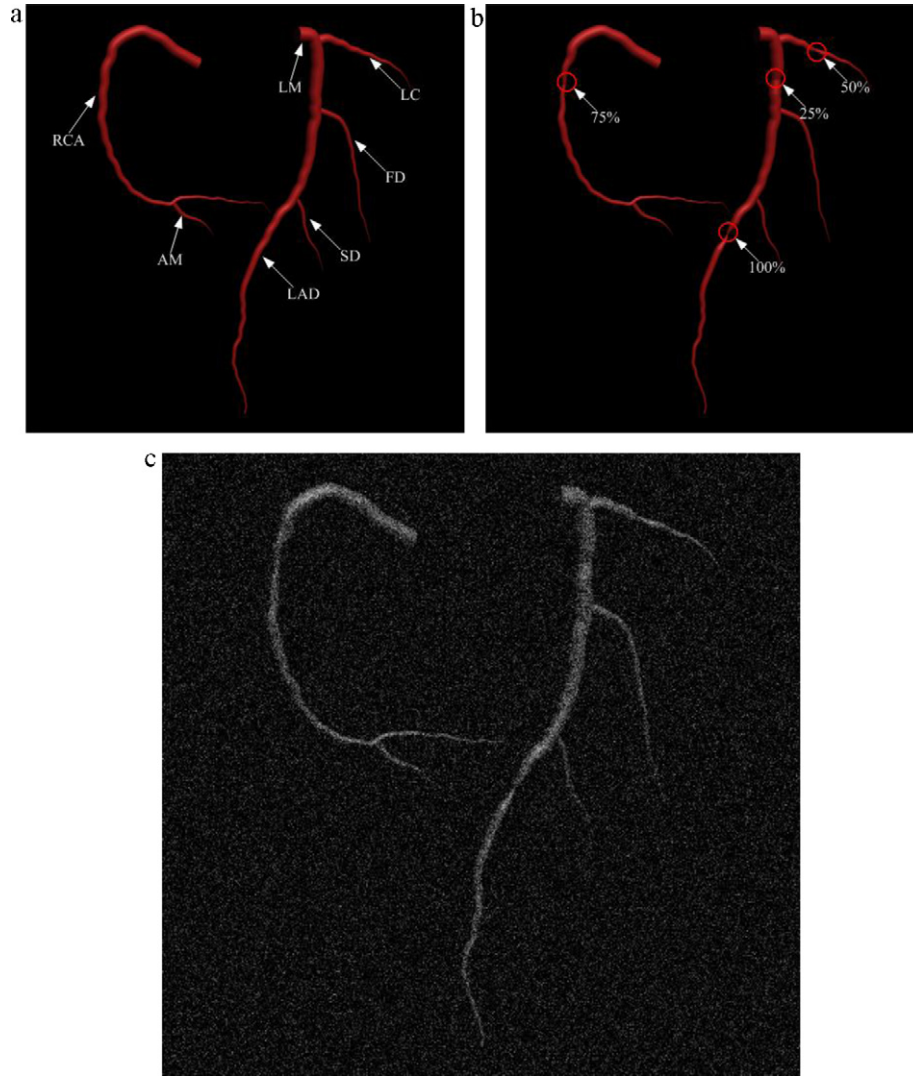
Fig. 4. Illustration of stenosis simulation. (a) A simulated 3D coronary artery tree and labeling of different branches – right coronary tree: right coronary artery (RCA) and acute marginal (AM); left coronary tree: left main coronary artery (LM), proximal left anterior descending artery (LAD), first diagonal (FD), second diagonal (SD) and proximal left circumflex artery (LC). (b) An example of simulated stenoses on the original phantom data of (a). Locations and severity of stenoses are marked. (c) A maximum intensity projection (MIP) of the image of (b) in the presence of partial voluming and noise.

degrees of severity is presented in Fig. 4(b) and (c). Stenoses of different severities – 25%, 50%, 75%, and 100% – were randomly simulated on different branches of a coronary arterial tree. A total of 20 simulated coronary artery phantom images were generated from the five initial healthy phantoms. The number of stenoses on each image was randomly selected between one and five and at most one stenosis was selected on each branch. Also, the arterial branch and the location of a stenosis on the branch were both selected randomly.

Stenoses on each phantom image were detected and graded using the algorithm described in Section 2. Finally, for each simulated (or, observed by a computerized method) stenosis γ, the matching observed (respectively, simulated) stenosis, if any, was identified and an error was computed as follows.

$$
error(\gamma) = \begin{cases} 1 - \dfrac{S_{observed}(\gamma)}{S_{simulated}(\gamma)}, & \text{if } S_{simulated} > S_{observed}, \\ \dfrac{S_{simulated}(\gamma)}{S_{observed}(\gamma)}, & \text{otherwise}, \end{cases}
$$

where $S_{simulated}(\gamma)$ denotes the simulated grade of the stenosis (γ) while $S_{observed}$ denotes the grade of (γ) computed by a computerized method; in case a simulated stenosis is missed by a computerized method, $S_{observed}$ is considered to be zero and vice versa.

3.2. A clinical study

To evaluate the performance of the proposed method from clinical perspective, an experimental study was designed on a clinical CTA database of thirteen patients (sex: 11 M and 2 F; mean and standard deviation of age: 53.6 Y and 9 Y). Patients were suffering from various vascular lesions and were scanned on a GE LightSpeed16 clinical CTA scanner under the following protocol −120 kVp, 400 mAs, patient position: brust, image matrix: 512×512, 80–110 slices, FOV: 22×22 cm^2, slice thickness: 1.25 mm, pixel size: 0.43×0.43 mm^2. Fuzzy segmentation of coronary arteries from CTA images was performed using a recently published coronary segmentation method by Yang et al. [15,17] prior to applying the stenosis detection/quantification algorithm presented in Section 2. Also, three expert clinicians independently identified and graded stenoses on each CTA as the percent measure of blockage (25%, 50%, 75% or 100%). A consensus grading from the three experts (described later) was used as the ground truth and was compared with the percent of stenosis measure produced by

the FDT-based computerized method. To compare the performance of the proposed method with the conventional [56] and BDT-based methods, the same experiment was run by replacing the FDT-based method with the respective method. In the following paragraphs we describe the methods for fuzzy segmentation of coronary artery and stenosis grading by a clinician.

3.2.1. Computation of a fuzzy representation of coronary arteries

Segmentation plays a crucial role in detection and quantification of coronary arterial stenoses and may be a research project on itself. Here, we have implemented the coronary artery segmentation method via CTA published by Yang et al. [15,17] who have also studied the robustness and accuracy of their method. An example of coronary artery segmentation and its 3D reconstruction are illustrated in Fig. 5(a) and (b). In order to capture the full extent of partial volume voxels, the original segmented region for arteries was dilated by one voxel; let A denote the set of voxels in segmented and then dilated arterial region. A fuzzy representation of the arterial tree was computed as follows:

$$\mu_A(p) = \begin{cases} 0, & \text{if } p \notin A \\ \dfrac{I_{CTA}(p) - I_{non\text{-}artery}}{I_{confident\text{-}artery} - I_{non\text{-}artery}} & I_{non\text{-}artery} \leq I_{CTA}(p) \leq I_{confident\text{-}artery}, \\ 1 & I_{CTA}(p) > I_{confident\text{-}artery}, \end{cases}$$

where I_{CTA} is the CTA intensity function and $I_{non\text{-}arter}$ and $I_{confident\text{-}artery}$ are the manually identified intensity values for non-artery and confident-artery voxels.

3.2.2. Grading of arterial stenosis by a clinician

CardIQ analysis software was used by each of three trained clinicians to interactively detect and grade stenoses in CTA images. These results were considered as the ground truth for evaluating the effectiveness of a computerized method. The following protocol was pursued for interactively detecting and grading stenoses using the CardIQ software.

(1) Reconstruct the 3D heart and coronary arteries and view using 3D volume rendering as illustrated in Fig. 6(a).
(2) Manually trace centerline of a pathological coronary artery and manually select the optimal angle to generate a two-dimensional curve reformatted view (see Fig. 6(b)).
(3) The vessel in the curved reformatted view is then straightened out using the analytic computing facilities within software generating the so-called 'lumen view' and measurements of the vessel diameter and area are reported (see Fig. 6(c)). Once a stenosis is recognized by the clinician, the measure of stenosis may be reported either in millimeter or as a percent of arterial blockage. The CardIQ software automatically generates local diameter and/or cross-sectional area measures. Both the region of a stenosis and expected local normal diameter are determined by the expert who calculates the latter by observing diameter values over normal regions at the vicinity of the stenosis.
(4) The above three steps are followed for each pathological arterial tree branch using the reference of center line and the graphical interface supported by the software.

Consensus grading of a stenosis was derived from its grades by three independent experts as follows. Let a, b, c be the percent grades by three experts for a given stenosis. Consensus grade of the stenosis is defined as

$$\text{consensus grade} = \underset{x \in \{0,25,50,75,100\}}{\arg\min} \left| x - \frac{a+b+c}{3} \right|,$$

i.e., the consensus grade falls under the category closest to the average of three expert grades. Also, the percent of variation among three experts under each category is defined as follows. Let a_i, b_i, $c_i | i = 1, \ldots, n_x$ be the stenosis grades by three experts for all stenoses under the category $x \in \{0, 25, 50, 75, 100\}$. Grade variation for a given category is defined as

$$\text{grade variation}(x) = \sqrt{\frac{1}{3n_x} \sum_{i=1}^{n_x} (a_i - x)^2 + (b_i - x)^2 + (c_i - x)^2}.$$

Finally, the overall grade variation among experts is defined as follows

overall grade variation

$$= \sqrt{\frac{1}{3 \sum_{x \in \{0,25,50,75,100\}} n_x} \sum_{x \in \{0,25,50,75,100\}} \sum_{i=1}^{n_x} (a_i - x)^2 + (b_i - x)^2 + (c_i - x)^2}.$$

Finally, for each consensus (or, detected by a computerized method) stenosis γ, the matching computer-detected (respectively, consensus) stenosis, if any, was identified and an error was computed as follows.

$$\text{error}_{clinical}(\gamma) = |S_{detected}(\gamma) - S_{consensus}(\gamma)|,$$

where $S_{detected}(\gamma)$ denotes the computer-detected grading of the stenosis γ while $S_{consensus}$ denotes the consensus grading of γ; in case a consensus stenosis is missed by a computerized method, $S_{detected}$ is considered to be zero and vice versa. The overall error was determined by adding $\text{Error}_{clinical}$ for all stenoses and then dividing it by the number of consensus stenoses.

4. Results and discussion

Results of application of different stages of the proposed method are illustrated in Fig. 5. It may be noted that, despite the presence of significant unevenness along the arterial surface in Fig. 5(b), the noise cleaned curve skeleton appears to be free of noisy branches. The performance of the proposed noise cleaning algorithm, also demonstrated in Fig. 1, has been found to be satisfactory in our applications on all data sets used for the current experimental set up. The noise cleaning algorithm along with the FDT technology has significantly enhanced the robustness and accuracy of our approach as may be visually observed in the examples illustrated in Figs. 5 and 7.

Accuracy of the proposed method has been quantitatively evaluated using the simulated stenosis phantom dataset and the error measure described in Section 3.1. Results of comparison between the three methods for different severity of stenosis and different anatomic arterial branches are presented in Fig. 8. Average errors by the new FDT- and BDT-based and the conventional methods are 0.53%, 2.11% and 3.71%, respectively, showing that the new method reduces stenosis quantification errors by four to sevenfold as compared to the BDT-based and conventional methods.

Results of stenosis grading by three independent experts are shown in Table 2. The study involved a database of clinical CTA of thirteen heart patients. Altogether 60 consensus stenoses were detected by the three experts. One expert detected an extra stenosis with 25% grade. Except for the first category, percent variation was less than 10%; overall percent variation among three experts was
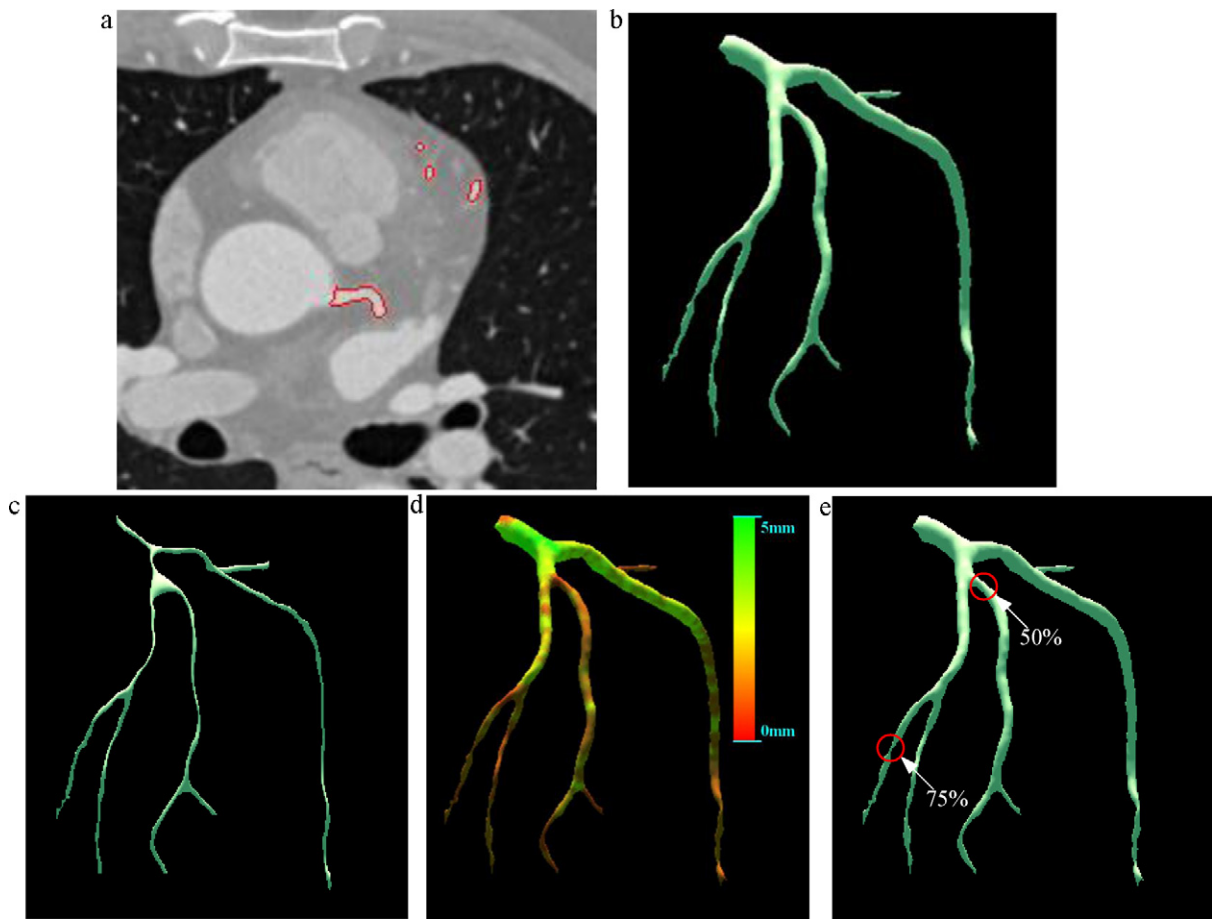
Fig. 5. Results of FDT-based computerized coronary arterial stenosis quantification via CTA. (a) A slice image from a CTA image acquired at $0.43 \times 0.43 \times 1.25$ mm^3 resolution along with boundaries of segmented coronary arteries. (b) 3D rendition of the left coronary artery tree derived from CTA. (c) The medial axis representation of the coronary artery tree after applying skeletal pruning. (d) A color-coded display of observed local diameter in 3D coronary artery tree; the color scale is shown. (e) FDT-based detection and quantification of stenoses. (For interpretation of the references to color in this figure legend, the reader is referred to the web version of this article.)

7.68%. Results of a comparative study of coronary arterial stenosis quantification by the two computerized methods and that by three experts using the CardIQ software are presented in Table 3. In both tables, the abscissa denotes consensus grades of stenoses by three independent experts while the ordinate indicates the grades generated by a computerized method. Here, it may be pointed out that not all stenoses detected in this study satisfy the clinical definition. Generally, for most clinical diagnostic purpose, a stenosis constitutes 70% or more arterial blockage. Here, we intentionally detect

stenoses with lesser blockage to examine the performance of the method at early stage of disease.

Table 3(a) presents the performance of the new FDT-based method in terms of its agreement with the experts grading of stenoses while Table 3(b) and (c) present the same but for the BDT-based and conventional methods. In all three tables, zero percent stenosis is used to represent false positives and false negatives of computerized stenosis detection algorithms. Table 3(a) shows that the FDT-based computerized method produced only one case of
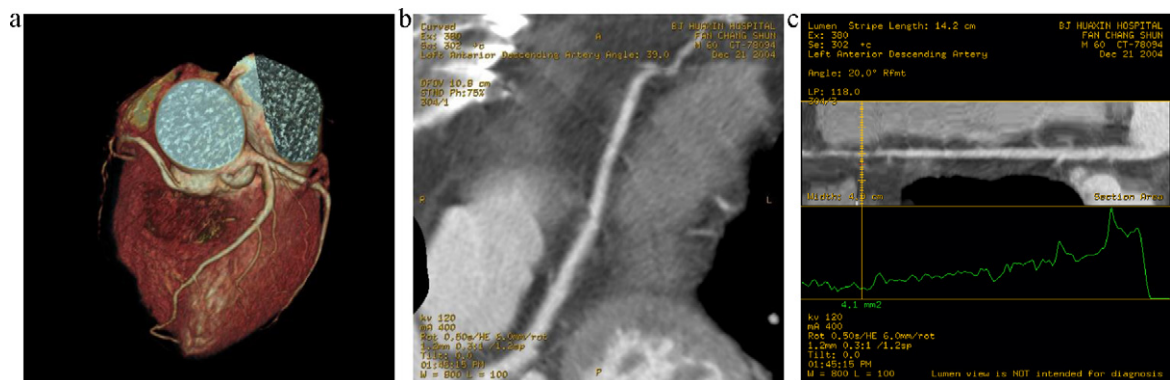

Fig. 6. Illustration of the graphical user interface supported by the CardIQ software for detecting and grading coronary arterial stenoses. (a) 3D reconstruction of heart and coronary arteries. (b) The graphical view using the curved image reformatting. (b) The lumen view and the measurement of local diameter profile (green) along the arterial central line. (For interpretation of the references to color in this figure legend, the reader is referred to the web version of this article.)
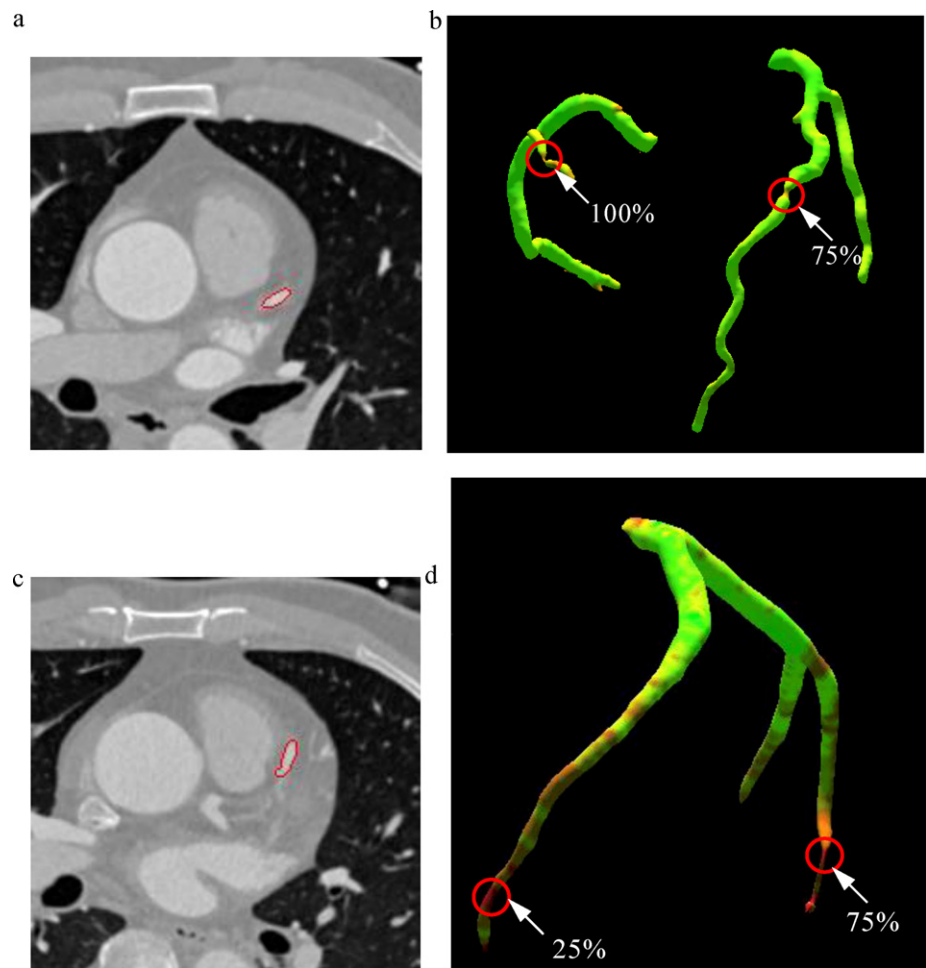
Fig. 7. Illustrations of more results of coronary artery stenosis quantification. (a) A slice image from a CTA dataset acquired at $0.43 \times 0.43 \times 1.25\,\text{mm}^3$ resolution along with boundaries of segmented coronary arteries. (b) Detection and quantification of stenoses. (c and d) Same as (a) and (b) but for CTA of another patient.

false positive (i.e., marked a stenosis with zero consensus grading) and one case of false negative (i.e., missed a stenosis with ≥25% consensus grading) while these numbers for BDT-based and the conventional method are 1, 2 and 1,3, respectively (Table 3(b) and (c)). For all three tables, large numbers appear at diagonal cells and a few small numbers adhere to adjacent cells. This observation demonstrates good agreement between computerized grading of stenoses and that by an expert. However, the values at diagonal

cells in Table 3(a) are always greater than corresponding values in Table 3(b) and (c) demonstrating that the FDT-based method produces larger agreement with the expert's stenosis quantification as compared to the BDT-based and conventional methods. We computed kappa coefficients [60,61] for Table 3(a)–(c) and the values observed are 87.9%, 75.2% and 69.5%, respectively, showing that the FDT based method is in better agreement with the consensus grading as compared to the BDT-based and conventional methods.

It may be observed in all three tables that computerized methods slightly underestimate the grades of stensoses as compared to the experts' grading which may be explained as follows. Plaque and calcium deposits in coronary artery tree change local intensities resulting in errors in FDT-based diameter computation. Intensities of plaque and calcium deposits are brighter than that of the normal vessel producing artifactual increase in FDT values and over estimating local diameters of coronary artery leading to under esti-
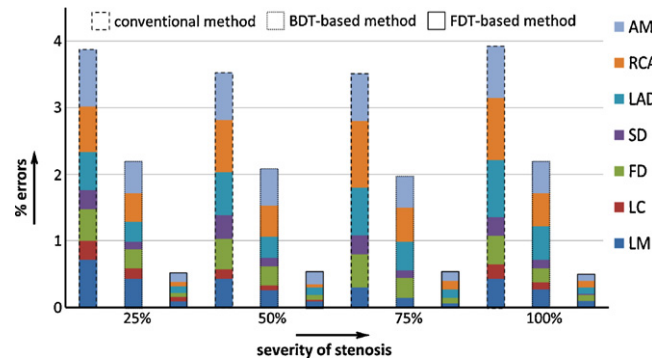

Fig. 8. An illustrative comparison of performances by the current FDT- and BDT-based and conventional methods for quantifying coronary arterial stenoses in simulated realistic phantoms. Here, the total height of each bean represents the average percentage error by a specific method at a particular severity of stenosis; the height of each color band in a given bin indicates the percent error committed on a specific arterial branch.

Table 2
Results of quantitative stenosis grading by three independent observers using the CardIQ software. The first column lists the stenosis grades, while the second one lists their consensual counts; the third column shows variations among three experts under each category.

Stenosis grade (%)	Consensus counts	Grade variation (%)
0	1	14.43
25	22	5.33
50	22	9.23
75	9	8.33
100	6	5.89

Table 3

Comparative results of coronary arterial stenosis detection and quantification on a CTA database of thirteen heart patients. (a) The confusion matrix comparing agreements of stenoses quantification by the FDT-based method and an expert using the CardIQ software. (b and c) Same as (a) but for the BDT-based and conventional methods.

	Consensus grading of stenoses by three experts				
	0%	25%	50%	75%	100%
(a) FDT-based computerized stenosis detection/grading					
0%		1			
25%	1	20	2		
50%		1	19	1	
75%			1	8	
100%					6
(b) BDT-based computerized stenosis detection/grading					
0%		2			
25%	1	18	4		
50%		2	17	1	
75%			1	7	2
100%				1	4
(c) Conventional computerized stenosis detection/grading					
0%		3			
25%	1	16	5		
50%		3	16	1	
75%			1	7	2
100%				1	4

mate in stenosis grading. It may be a shortcoming of a computerized automatic stenosis quantification method and may be overcome by improving the fuzzy segmentation method for arterial tree.

Overall, a new method for quantifying coronary arterial stenosis via CTA using fuzzy distance transform method has been presented. A new skeletal pruning algorithm has been developed toward improving quality of medial axis of a coronary which significantly enhances the accuracy of quantification of coronary arterial stenosis. Also, a new algorithm has been presented for determining expected arterial diameters along an arterial branch from observed values based on finding a set of coherent observed diameters. The algorithm has been found to be successful in eliminating the effects of the depression in observed diameters caused by a stenosis ensuring that expected diameters are computed from observed diameters over healthy regions only. At the same time, the algorithm creates no bias for healthy branches. The accuracy of the method has been evaluated using both realistic simulated phantoms and CTA datasets from thirteen heart patients and by comparing with manual identification and grading of stenosis. The method has been compared with the conventional and BDT-based methods. Comparative experimental results with the two methods have demonstrated the benefits of using FDT together with a new *SDT*-based pruning and the approach of stenosis grading based on expected/observed diameters. Although the new method compares very favorably with the selected existing methods, the gap may be smaller if compared with more recent methods. In the current non-optimized implementation the new FDT based stenosis detection and quantification method takes approximately 1 min for each patient CTA dataset running on an Intel Core PC with 2.33 Hz Intel(R) 2 Duo CPU and 2G RAM memory. The conventional binary method takes approximately 5 min for each dataset where most time is required to compute cross-sectional area in the orthogonal plane.

Acknowledgements

References

[1] Xu Y, Hu GS, Geng JZ, Shang LH. Automated coronary arterial tree extraction using parallel and topology. Chin J Biomed Eng 2007;26:24–9.

[2] Fayad ZA, Fuster V, Nikolaou K, Becker C. Computed tomography and magnetic resonance imaging for noninvasive coronary angiography and plaque imaging: current and potential future concepts. Circulation 2002;106:2026–34.

[3] Lesser JR, Knickelbine T, Chavez I, Lindberg J, Schwartz RS. Ruptured plaque visualization by noninvasive coronary computed tomography angiography. Circulation 2004;110:e311–2.

[4] Hoffmann MH, Shi H, Schmitz BL, Schmid FT, Lieberknecht M, Schulze R, et al. Noninvasive coronary angiography with multislice computed tomography. JAMA 2005;293:2471–8.

[5] Tanaka N, Ehara M, Surmely JF, Matsubara T, Terashima M, Tsuchikane E, et al. Sixty-four-multislice computed tomography image of a ruptured coronary plaque. Circulation 2006;114:e519–20.

[6] Cho ZH, Jones JP, Singh M. Foundation of medical imaging. New York: Wiley; 1993.

[7] Cordeiro MA, Lardo AC, Brito MS, Rosario Neto MA, Siqueira MH, Parga JR, et al. CT angiography in highly calcified arteries: 2D manual vs. modified automated 3D approach to identify coronary stenoses. Int J Cardiovasc Imaging 2006;22:507–16.

[8] Sun J, Zhang Z, Lu B, Yu W, Yang Y, Zhou Y, et al. Identification and quantification of coronary atherosclerotic plaques: a comparison of 64-MDCT and intravascular ultrasound. Am J Roentgenol 2008;190:748–54.

[9] Hur J, Kim YJ, Lee HJ, Nam JE, Choe KO, Seo JS, et al. Quantification and characterization of obstructive coronary plaques using 64-slice computed tomography: a comparison with intravascular ultrasound. J Comput Assist Tomogr 2009;33:186–92.

[10] Blackmon KN, Streck J, Thilo C, Bastarrika G, Costello P, Joseph Schoepf U. Reproducibility of automated noncalcified coronary artery plaque burden assessment at coronary CT angiography. J Thorac Imaging 2009;24:96–102.

[11] Bekkers E, Roos J. Coronary CTA: stenosis classification and quantification, including automated measures. J Cardiovasc Comput Tomogr 2009;3(Suppl. 2):S109–15.

[12] Riedel CH, Chuah SC, Zamir M, Ritman EL. Accurate segmentation for quantitative analysis of vascular trees in 3D micro-CT images. In: Proceedings of SPIE: medical imaging. 2002. p. 256–65.

[13] Florin C, Paragios N, Williams J. Particle filters, a quasi-Monte-Carlo-solution for segmentation of coronaries. Med Image Comput Comput Assist Interv Int Conf Med Image Comput Comput Assist Interv 2005;8:246–53.

[14] Szymczak A, Stillman A, Tannenbaum A, Mischaikow K. Coronary vessel trees from 3D imagery: a topological approach. Med Image Anal 2006;10:548–59.

[15] Yang Y, Tannenbaum A, Giddens D, Wallace H. Knowledge-based 3D segmentation and reconstruction of coronary arteries using CT images. In: Presented at the 26th annual international conference of the IEEE engineering in medicine and biology society. 2004.

[16] Yang Y, Zhu L, Haker S, Tannenbaum AR, Giddens DP. Harmonic skeleton guided evaluation of stenoses in human coronary arteries. In: Presented at the int conf med image comput comput assist interv. 2005.

[17] Yang Y, Tannenbaum A, Giddens D, Stillman A. Automatic segmentation of coronary arteries using Bayesian driven implicit surfaces. In: Proceedings of 4th IEEE international symposium on biomedical imaging. 2007. p. 189–92.

[18] Wang C, Frimmel H, Persson A, Smedby Ö. An interactive software module for visualizing coronary arteries in CT angiography. Int J Comput Assist Radiol Surg 2008;3:11–8.

[19] Antiga L, Ene-Iordache B, Caverni L, Cornalba GP, Remuzzi A. Geometric reconstruction for computational mesh generation of arterial bifurcations from CT angiography. Comput Med Imaging Graph 2002;26:227–35.

[20] Antiga L, Ene-Iordache B, Remuzzi A. Computational geometry for patient-specific reconstruction and meshing of blood vessels from MR and CT angiography. IEEE Trans Med Imaging 2003;22:674–84.

[21] Chen Z, Molloi S. Automatic 3D vascular tree construction in CT angiography. Comput Med Imaging Graph 2003;27:469–79.

[22] Boskamp T, Rinck D, Link F, Kummerlen B, Stamm G, Mildenberger P. New vessel analysis tool for morphometric quantification and visualization of vessels in CT and MR imaging data sets. Radiographics 2004;24:287–97.

[23] Rosenfeld A. Fuzzy digital topology. Inf Control 1979;40:76–87.

[24] Rosenfeld A. The fuzzy geometry of image subsets. Pattern Recognit Lett 1991;2:311–7.

[25] Udupa JK, Samarasekera S. Fuzzy connectedness and object definition: theory, algorithms, and applications in image segmentation. Graph Models Image Process 1996;58:246–61.

[26] Saha PK, Udupa JK. Scale-based fuzzy connectivity: a novel image segmentation methodology and its validation. In: Proceedings of SPIE: medical imaging. 1999. p. 246–57.

[27] Saha PK, Udupa JK. Relative fuzzy connectedness among multiple objects: theory, algorithms, and applications in image segmentation. Comput Vis Image Underst 2001;82:42–56.

[28] Lesage D, Angelini ED, Bloch I, Funka-Lea G. A review of 3D vessel lumen segmentation techniques: models, features and extraction schemes. Med Image Anal 2009;13:819–45.

[29] Saha PK, Wehrli FW, Gomberg BR. Fuzzy distance transform: theory, algorithms, and applications. Comput Vis Image Underst 2002;86:171–90.

[30] Rosenfeld A, Pfaltz J. Distance functions in digital pictures. Pattern Recognit 1968;1:33–61.

[31] Daniensson PE. Euclidean distance mapping. Comput Graph Image Process 1980;14:227–48.
[32] Okabe N, Toriwaki J, Fukumura T. Paths and distance functions in three dimensional digitized pictures. Pattern Recognit Lett 1983;1:205–12.
[33] Borgefors G. Distance transform in arbitrary dimensions. Comput Vis Graph Image Process 1984;27:321–45.
[34] Borgefors G. Distance transformations in digital images. Comput Vis Graph Image Process 1986;34:344–71.
[35] Borgefors G. On digital distance transformation in three dimensions. Comput Vis Graph Image Process 1996;64:368–76.
[36] Klette R, Rosenfeld A. Digital geometry: geometric methods for digital picture analysis. San Francisco, CA: Morgan Kaufmann; 2004.
[37] Verwer BJH. Local distances for distance transformations in two and three dimensions. Pattern Recognit Lett 1991;12:671–82.
[38] Beckers ALD, Smeulders AWM. Optimization of length measurements for isotropic distance transformations in three dimension. CVGIP Image Underst 1991;55:296–306.
[39] Grevera GJ, Udupa JK. Shape-based interpolation of multidimensional grey-level images. IEEE Trans Med Imaging 1996;15:881–92.
[40] Saha PK, Wehrli FW. Measurement of trabecular bone thickness in the limited resolution regime of in vivo MRI by fuzzy distance transform. IEEE Trans Med Imaging 2004;23:53–62.
[41] Svensson S. Centres of maximal balls extracted from a fuzzy distance transform. In: Proceedings of 8th international symposium on mathematical morphology. 2007. p. 19–20.
[42] Svensson S. A decomposition scheme for 3D fuzzy objects based on fuzzy distance information. Pattern Recognit Lett 2007;28:224–32.
[43] Svensson S. Aspects on the reverse fuzzy distance transform. Pattern Recognit Lett 2008;29:888–96.
[44] Darabi A. Assessment of the porous media structure based on fuzzy distance transform and its map ridge. Magn Reson Imaging 2007;25:556–1556.
[45] Wehrli FW, Ladinsky GA, Jones C, Benito M, Magland J, Vasilic B, et al. In vivo magnetic resonance detects rapid remodeling changes in the topology of the trabecular bone network after menopause and the protective effect of estradiol. J Bone Miner Res 2008;23:730–40.
[46] Cachia A, Mangin J-F, Rivière D, Papadopoulos-Orfanos D, Kherif F, Bloch I, et al. A generic framework for the parcellation of the cortical surface into gyri using geodesic voronoï diagrams. Med Image Anal 2003;7:403–16.

[47] Chang G, Pakin SK, Schweitzer ME, Saha PK, Regatte RR. Adaptations in trabecular bone microarchitecture in Olympic athletes determined by 7 T MRI. J Magn Reson Imaging 2008;27:1089–95.
[48] Schaap M, Metz CT, van Walsum T, van der Giessen AG, Weustink AC, Mollet NR, et al. Standardized evaluation methodology and reference database for evaluating coronary artery centerline extraction algorithms. Med Image Anal 2009;13:701–14.
[49] Saha PK, Rosenfeld A. Determining simplicity and computing topological change in strongly normal partial tilings of R^2 or R^3. Pattern Recognit 2000;33:105–18.
[50] Saha PK, Chaudhuri BB. 3D digital topology under binary transformation with applications. Comput Vis Image Underst 1996;63:418–29.
[51] Saha PK, Chaudhuri BB, Majumder DD. A new shape preserving parallel thinning algorithm for 3D digital images. Pattern Recognit 1997;30:1939–55.
[52] Saha PK, Chaudhuri BB, Chanda B, Majumder DD. Topology preservation in 3D digital space. Pattern Recognit 1994;27:295–300.
[53] Saha PK, Chaudhuri BB. Detection of 3D simple points for topology preserving transformation with application to thinning. IEEE Trans Pattern Anal Mach Intell 1994;16:1028–32.
[54] Xu Y, Saha PK, Hu G, Liang G, Yang Y, Geng J. Quantification of stenosis in coronary artery via CTA using fuzzy distance transform. In: Presented at the SPIE: medical imaging. 2009.
[55] Dodge JT, Brown BG, Bolson EL, Dodge HT. Lumen diameter of normal human coronary arteries. Influence of age, sex, anatomic variation, and left ventricular hypertrophy or dilation. Circulation 1992;86:232–46.
[56] Bühler K, Felkel P, Cruz AL. Geometric methods for vessel visualization and quantification – a survey. In: Brunnett BHG, Müller H, editors. Geometric modelling for scientific visualization. Springer; 2003. p. 399–421.
[57] Leung WH, Stadius ML, Alderman EL. Determinants of normal coronary artery dimensions in humans. Circulation 1991;84:2294–306.
[58] Chalopin C, Finet G, Magnin IE. Modeling the 3D coronary tree for labeling purposes. Med Image Anal 2001;5:301–15.
[59] Xue P, Wilson DL. Detection of moving objects in pulsed-X-ray fluoroscopy. J Opt Soc Am A 1998;15:375–88.
[60] Cohen J. Weighed kappa: nominal scale agreement with provision for scaled disagreement or partial credit. Psychol Bull 1968;70:213–20.
[61] Cohen J. A coefficient of agreement for nominal scales. Educ Psychol Meas 1960;20:37–46.